

Short Papers

Improvement of Design and Motion Control for Motion Platform Based on Spherical Wheels

Seong-Min Lee  and Hungsun Son , *Member, IEEE*

Abstract—In this paper, a six-degree-of-freedom (DOF) motion platform based on spherical wheels is presented to improve design and motion control from the earlier design. The motion platform developed here is capable of 3-DOFs unlimited rotation and 3-DOFs translation, which has large workspace of linear motion with better stability and high rigidity. In particular, the new design offers better motion control, uniformity, and safety in motion range by additional actuators providing better motion capability for virtual reality. Kinematic analysis of the platform is investigated to provide a basis for motion controllability. In particular, the rotational motion can be independently controlled from the translation by the active driving control. The design and motion analysis are demonstrated from both numerical simulation and experiment using a prototype in an open-loop control. Slipping motion and friction as a main driving torque are experimentally evaluated for a nonslip condition. The comparison results prove the design feasibility and motion control capability.

Index Terms—Kinematic analysis, motion platform, multi-degree-of-freedom (DOF) motion control, spherical wheels.

I. INTRODUCTION

Multi-degree-of-freedom (DOF) motion generation has been explored in various research fields, such as manipulator [1], multi-agent system [2], haptic device [3], three-dimensional print [4], and exoskeleton for rehabilitation [5]. In particular, the motion capability having unlimited motion range becomes more significant. However, existing research papers using serial and parallel mechanisms have been widely used but have some limitations. The serial platforms [1] have large workspace, low rigidity, and large inertia. On the other hand, the parallel platforms [2]–[5] have advantages of high rigidity and stability but smaller workspace and higher complexity than the serial platforms.

To overcome the limitations of the serial and parallel platforms, various research papers have been proposed by utilizing additional actuators [3], [6]–[8]. The redundancy enhances the motion capability with the larger force and torque. However, most available mechanisms

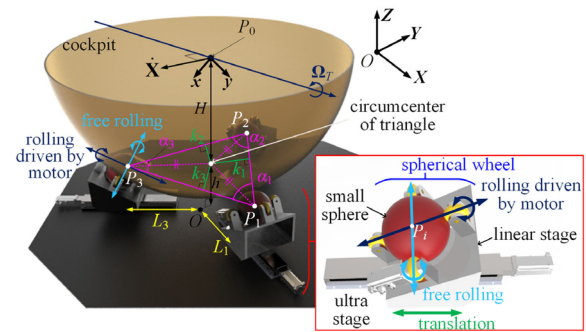


Fig. 1. Design and mechanical structures of the motion platform I.

with additional actuators still suffer for limitations such as small workspace [3], [8] and high complexity [6], [7]. The novel designs involving unlimited motion capability have been proposed to solve a small motion range. The spherical wheel motor for 3-DOFs rotation [9] capable of unlimited motion in only yaw has been developed. The Atlas [10] is a motion platform performing 6-DOFs motion with 3-DOFs unlimited rotation for all axes driven by omniwheels, and the rotational system is installed on a Stewart platform [11] to produce 3-DOFs translation with six actuators. The omniwheels can generate unnatural motion owing to discontinuity caused by their geometric characteristics. Furthermore, parallel mechanism for the translation can cause high complexity and motion coupling. As a result, the motion platform becomes bulky, complex, and redundant.

The development of the motion platform based on the spherical wheels has been explored [12], as shown in Fig. 1. It can generate 6-DOFs motion with 3-DOFs unlimited rotation and 3-DOFs translation with smooth motion transfer from the spherical wheel. The platform has better rigidity maintaining contact and minimizing slippage from the spherical wheels compared to omniwheels causing discontinuity. Moreover, the design will be more compact and bring cost efficiency since the rotational and translational systems are combined. However, the motion platform based on the spherical wheels can suffer geometric instability causing the escape of the cockpit and the coupled motion between the translation and rotation. As a result, the workspace and motion capability decrease incurring unnatural motion. A motion platform having four linear stages has been introduced in [13]. The proposed design improves reachable workspace, allowable motion capability, and motion efficiency using simplified geometry.

This paper presents a kinematic and dynamic analysis of a spherical wheel motion platform with geometric stability and friction analysis with experiments compared to the previous [12]. An open-loop control based on active driving control is proposed to compensate the coupled motion. The remainder of this paper is organized as follows.

Manuscript received November 2, 2018; revised February 27, 2019 and June 1, 2019; accepted July 29, 2019. Date of publication August 7, 2019; date of current version October 15, 2019. This work was supported in part by the Future Innovation Research Funds (1.190003.01) of the Ulsan National Institute of Science and Technology and in part by the Development of Multi-Degrees of Freedom Spherical Motion Platform (2.190080.01) of Civil Military Technology Cooperation Center. Recommended by Technical Editor J. Yi. (Corresponding author: Hungsun Son.)

The authors are with the School of Mechanical, Aerospace, and Nuclear Engineering, Ulsan National Institute of Science and Technology, Ulsan 44919, South Korea (e-mail: leesm128@unist.ac.kr; hson@unist.ac.kr).

Color versions of one or more of the figures in this article are available online at <http://ieeexplore.ieee.org>.

Digital Object Identifier 10.1109/TMECH.2019.2933553

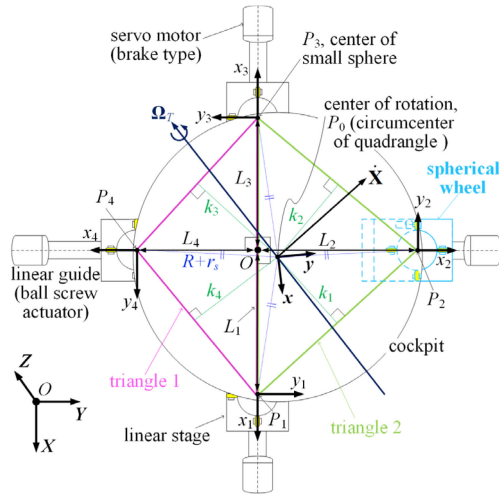


Fig. 2. Design and mechanical structures of the motion platform II [13].

- 1) First, the design and mechanical structure of a new motion platform consisting of four spherical wheels are presented. The motion platform can provide larger workspace for the translation with better stability compared to the design in Fig. 1.
- 2) The rotational motion is analyzed by computing inverse kinematics with a unique solution. Moreover, the rotational motion is decoupled from the translational motion by an active driving control compared to the earlier analysis in [12] and [13]. The friction force and the slip ratio are obtained to evaluate the rolling condition according to slipping. The kinematics is demonstrated from experiments in an open-loop control. The results validate the design and motion control performance of 6-DOFs motion.

II. MECHANICAL DESIGN

The motion platform in [13] using four driving spherical wheels is designed to control 3-DOFs rotational and 3-DOFs translational motions. Fig. 2 shows the conceptual and mechanical design referred hereto as motion platform II. It consists of three components: main sphere as a cockpit, four small spheres for driving rotation, and four linear stages for driving translation. The linear stages move along each linear guide installed with 90° separation angle on the base of the platform in contrast to platform I in Fig. 1. The spherical wheel for the main driving system is the same as the platform I. For the rotational motion, the design involves four small spheres to support and spin the cockpit. In addition, four motors are utilized to transfer the torque on the linear stages. The translational system consists of four linear stages with each motor on the linear guides and four small spheres rolling freely.

For operating mechanism, the rotational motion is driven by four small spheres and each small sphere is rotated along two directions, which are spinning driven by the motor and free rolling, as shown in Fig. 1. The cockpit sphere is reachable to full rotational workspace $\pm 180^\circ$. The translation is driven from the linear stages along with each linear guide changing contact points between the cockpit and the four small spheres. For guarantee of the mobility of the rotation and translation, the four contact points are essential and must be analyzed by kinematics. In addition, the coupling motion by the translation is caused by the characteristics of spherical wheels, but the coupled rotation can be compensated by the active driving control derived from the kinematic analysis.

III. KINEMATIC AND DYNAMIC ANALYSIS

The kinematics of the motion platform II can be expressed by the angular velocities of eight motors. An inertial frame with XYZ coordinates is defined at the intersection point of four linear stages on the base, and a body frame with xyz coordinates lies on the center of rotation (CR) of the cockpit, as shown in Fig. 2.

The position of the small spheres and the cockpit is defined for the motion analysis by geometric relation and analyzed in [13]. The center of the i th small sphere P_i in (1) and the position of the cockpit P_0 are computed in the inertial frame

$$P_i = [L_i \cos(\pi(i-1)/2) \quad L_i \sin(\pi(i-1)/2) \quad h]^T, i = 1, 2, 3, 4 \quad (1)$$

where L_i is the distance from the center O to the center of the i th small sphere; h is the height of the center of the small sphere from the base; P_0 becomes the circumcenter of quadrangle composed of $P_1 P_2 P_3 P_4$ as the circumcenters of two triangles calculated in (2a) and (2b) are coincident in order to satisfy four contact points. The relation of the circumcenter is used for obtaining the position of the cockpit. From the coincidence, the constraint equation is calculated as (3).

$$P_{0, \text{triangle1}} = 0.5 [L_1 - L_3 \quad (L_1 L_3 - L_4^2)/L_4 \quad 2(h + H_1)]^T \quad (2a)$$

$$P_{0, \text{triangle2}} = 0.5 [L_1 - L_3 \quad (L_2^2 - L_1 L_3)/L_2 \quad 2(h + H_2)]^T \quad (2b)$$

$$L_1 L_3 = L_2 L_4 \quad (3)$$

where the triangles 1 and 2 are $\Delta P_1 P_2 P_3$ and $\Delta P_1 P_3 P_4$, respectively; H_i is the height of the circumcenter of the i th triangle. As the four linear stages must satisfy constraint (3) to maintain four contact points and uniform weight distribution, P_0 in (4) can be rewritten from (2a) and (2b) as

$$P_0 = 0.5 [L_1 - L_3 \quad L_2 - L_4 \quad 2(h + H)]^T \quad (4)$$

$$H = \sum_{i=1}^2 \frac{1}{2} \sqrt{(R + r_s)^2 - \left(\frac{L_1 + (-1)^{i+1} L_3}{2} \right)^2 - \left(\frac{L_2 + (-1)^i L_4}{2} \right)^2} \quad (4a)$$

where r_s and R are the radii of the small sphere and the cockpit, respectively; H is the height of the CR of the cockpit from the center of the small sphere and can be obtained from (4a). The median value of H_1 and H_2 is caused by constraint (3) between L_i . In addition, L_i has geometric constraints

$$L_{\min} < L_1, L_2, L_3, \text{ and } L_4 < L_{\max} \quad (5)$$

where L_{\min} and L_{\max} are predetermined and equivalent to [12] for comparison of workspace between the platforms I and II.

A. Inverse Kinematics for the Rotation of the Cockpit

Rotation of the cockpit is driven by four motors through four small spheres to the cockpit sphere by considering the slip condition. Although the minimum number of small spheres is three for control, four driving systems offer better controllability and stability due to symmetry. Moreover, an accident from the faulty motor can be safely operated. The required rotation of each motor can be calculated from inverse kinematics applying the symmetric geometry. In order to obtain the rotation of the cockpit, the angular velocity of the cockpit

Ω_i driven from the i th motor can be expressed as

$$\Omega_i = \begin{cases} \frac{\lambda a_i r_w d_1}{\sqrt{2}R} \left[(-1)^{i+1} \left(\frac{1}{d_1} + \frac{L_1 + L_3}{2} \right) \quad \frac{L_4 - L_2}{2} \quad \frac{1}{d_1} - H \right]^T, & i = 1, 3 \\ \frac{\lambda a_i r_w d_2}{\sqrt{2}R} \left[\frac{L_3 - L_1}{2} \quad (-1)^i \left(\frac{1}{d_2} + \frac{L_2 + L_4}{2} \right) \quad \frac{1}{d_2} - H \right]^T, & i = 2, 4 \end{cases} \quad (6)$$

where $d_k = (2H - L_k - L_{k+2})/2(R + r_s)^2$, $k = 1, 2$; a_i is the i th motor input as the angular velocity; r_w is the radius of the roller; λ is the slip ratio ($= \theta_2/\theta_1$) between θ_2 rolling angles of the cockpit and θ_1 small sphere, namely, $\lambda = 0$ and 1 represent pure slip and pure rolling, respectively. It is assumed that the ratio is the same for all contact points because the linear stages are arranged from (3) to maintain the contact for uniform weight distribution. The rotation of the cockpit along the X-axis in (7a) can be calculated from the sum of (6). The motor input is set to be $a_1 = -a_3$ and $a_2 = a_4 = 0$. Then, the Y and Z components of (6) are canceled and the cockpit can obtain pure rotation along the X-axis. The rotation of the cockpit along the Y-axis (7b) can be determined from (6) in the same way setting as $a_2 = -a_4$ and $a_1 = a_3 = 0$. The motor input vectors of the rotation along X and Y axes are computed as $\mathbf{a}_X = [a_1 \ 0 \ -a_1 \ 0]^T$ and $\mathbf{a}_Y = [0 \ a_2 \ 0 \ -a_2]^T$, respectively

$$\Omega_X = a_1 r_w \lambda (2 + (L_1 + L_3) d_1) / \sqrt{2}R \quad (7a)$$

$$\Omega_Y = a_2 r_w \lambda (2 + (L_2 + L_4) d_2) / \sqrt{2}R. \quad (7b)$$

In particular, the rotation of the cockpit along the Z-axis can be computed from superposition of three components: generation of the rotation along the Z-axis and cancellation of the rotation along the X and Y axes. First, it is set to be $a_1 = a_3$ and $a_2 = a_4$ for a desired rotation Ω_Z along the Z-axis and sum of all driving inputs from (6). It is expressed in (8a)–(8c). Then, the undesired rotation Ω'_X and Ω'_Y in (9) along the X and Y axes can be removed from counter rotation. Finally, the cockpit is rotating only at Ω_Z without Ω'_X and Ω'_Y in (9)

$$\Omega_1 + \Omega_3 = (\lambda a_1 r_w / \sqrt{2}R) [0 \ (L_4 - L_2) d_1 \ 2 - 2H d_1]^T \quad (8a)$$

$$\Omega_2 + \Omega_4 = (\lambda a_2 r_w / \sqrt{2}R) [(L_3 - L_1) d_2 \ 0 \ 2 - 2H d_2]^T \quad (8b)$$

$$a_1 (1 - H d_1) = (1 - H d_2) a_2 \quad (8c)$$

$$\begin{bmatrix} \Omega'_X \\ \Omega'_Y \\ \Omega_Z \end{bmatrix} = \begin{bmatrix} (L_3 - L_1)(1 - H d_1) d_2 / (1 - H d_2) \\ (L_4 - L_2) d_1 \\ (2 - 2H d_1) \end{bmatrix} \frac{\lambda r_w a_1}{\sqrt{2}R}. \quad (9)$$

Once the desired angular velocity along the Z-axis is obtained, the motor input vector corresponding to the rotation can be computed from (7a), (7b), and (9), and expressed in (10)–(12). The motor input vectors \mathbf{a}_X and \mathbf{a}_Y in (10) and (11) are for the undesired rotation Ω'_X and Ω'_Y in (9). Equation (12) indicates the motor input vector for the desired

rotation Ω_Z .

$$\mathbf{a}_X = \frac{R(L_3 - L_1) d_2}{\sqrt{2} r_w \lambda (1 - H d_2) (2 + (L_1 + L_3) d_1)} \Omega_Z [-1 \ 0 \ 1 \ 0]^T \quad (10)$$

$$\mathbf{a}_Y = \frac{R(L_4 - L_2) d_1}{\sqrt{2} r_w \lambda (1 - H d_1) (2 + (L_2 + L_4) d_2)} \Omega_Z [0 \ -1 \ 0 \ 1]^T \quad (11)$$

$$\mathbf{a}_Z = \frac{\sqrt{2}R}{r_w \lambda (2 - 2H d_1)} \Omega_Z \left[1 \ \frac{1-H d_1}{1-H d_2} \ 1 \ \frac{1-H d_1}{1-H d_2} \right]^T. \quad (12)$$

B. Decoupled Motion by Active Driving Control

The translational motion as the linear velocity of the cockpit $\dot{\mathbf{X}}$ is expressed in terms of $\dot{\mathbf{L}}$ as

$$\dot{\mathbf{X}} = \mathbf{\Gamma} \dot{\mathbf{L}} \quad (13)$$

$$\mathbf{\Gamma}_{k,i} = \partial P_{0,k} (L_1, L_2, L_3, L_4) / \partial L_i, \quad k = 1, 2, 3 \text{ and } i = 1, 2, 3, 4 \quad (13a)$$

$$\dot{\mathbf{L}} = \mathbf{\Gamma}^T (\mathbf{\Gamma} \mathbf{\Gamma}^T)^{-1} \dot{\mathbf{X}}. \quad (13b)$$

Each component in (13a) is computed from (4); $\dot{\mathbf{L}} = [\dot{L}_1 \ \dot{L}_2 \ \dot{L}_3 \ \dot{L}_4]^T$ represents linear velocities of linear guides, as shown in Fig. 1. $P_{0,k}$ is the X, Y, and Z components of the position of the cockpit.

As the cockpit sphere has translational motion, the cockpit rotates according to free rotation of small spheres, as shown in Fig. 1. The rotation of the cockpit Ω_T due to the translation $\dot{\mathbf{X}}$ can be expressed as

$$\Omega_T = \sum_{i=1}^{N_a} \Omega_{T,i} \quad (14)$$

$$\Omega_{T,i} = (R \mathbf{P}_{0i} / \|\mathbf{P}_{0i}\|) \times \dot{\mathbf{X}}, \quad i = 1, \dots, N_a \quad (14a)$$

where $\Omega_{T,i}$ represents the angular velocity caused by the translation of the i th linear stage; N_a is determined to 3 and 4 about platforms I and II, respectively. The angular velocity of the cockpit due to the translation can be calculated from the sum of the vector cross product of $R \mathbf{P}_{0i} / \|\mathbf{P}_{0i}\|$ and $\dot{\mathbf{X}}$, as shown in Fig. 1. $R \mathbf{P}_{0i} / \|\mathbf{P}_{0i}\|$ is the vector of the cockpit radius from the i th contact point to the CR of the cockpit.

The coupled rotation can be compensated by the active driving control of driving spheres without any external sensors measuring orientation. The motor input \mathbf{a}_C for the active driving control to compensate the undesired motion coupling can be obtained as

$$\mathbf{a}_C = [\mathbf{N}]^{-1} [R(\mathbf{P}_{01} + \dots + \mathbf{P}_{0N_a}) / (R + r_s)] \times \dot{\mathbf{X}} \quad (15)$$

where \mathbf{N} represents the counter rotation about Ω_T occurred by motion coupling. In (15), the motor input as the angular velocity is computed from each inverse kinematics for the motion platforms I and II, respectively.

C. Geometric Stability

The motion platforms based on the spherical wheels have unlimited rotation, but the workspaces of the translation are determined from L_i in geometric limits in (5). The workspace can be decreased due to geometric stability to prevent the escape of the cockpit from contact with small spheres causing uncontrollable operation. The geometric stability is determined from whether the center of mass (CM) of the cockpit is located inside of the region composed of centers of small spheres.

In the motion platform I in Fig. 1, the region becomes triangle $\Delta \mathbf{P}_1 \mathbf{P}_2 \mathbf{P}_3$ and then the location of the CR of the cockpit, which is the circumcenter of the triangle, is computed from the internal angle as (16) when the CR is coincide with the CM of the cockpit

$$\max(\alpha_1, \alpha_2, \alpha_3) < 90^\circ \quad \forall L_1, L_2, L_3 \quad (16)$$

$$\alpha_i = \cos^{-1} (\mathbf{P}_{i,i+1} \bullet \mathbf{P}_{i,i+2} / (\|\mathbf{P}_{i,i+1}\| \|\mathbf{P}_{i,i+2}\|)), i = i + 2 \quad (16a)$$

where α_i , which is an angle between $\mathbf{P}_{i,i+1}$ and $\mathbf{P}_{i,i+2}$, can be computed from (16a), where $\mathbf{P}_{i,i+1} = \mathbf{P}_{i+1} - \mathbf{P}_i$, $i = 1, 2, 3$. When the maximum value among α_i becomes larger than 90° , the position of the cockpit center lies outside of the obtuse triangle incurring the cockpit becomes uncontrollable. In the motion platform I, the cockpit center is always located inside the triangle, from the result (16) assuming no torque caused from eccentricity between the CR and CM of the cockpit. However, in actual applications, eccentric load caused by human on board, electrical devices, and mechanical errors can make the cockpit uncontrollable due to loss of three contact points. The eccentric margin K for the cockpit sphere is computed as

$$K = \min(k_1, \dots, k_{N_a}) \quad (17)$$

$$k_i = \|\mathbf{P}_{i+1,i} \times \mathbf{P}_{0i}\| / \|\mathbf{P}_{i+1,i}\| \quad (17a)$$

where the k_i is the distance from the \mathbf{P}_0 to the $\mathbf{P}_{i,i+1}$ in the motion platform I, as shown in Fig. 1 and can be calculated from (17a).

For the motion platform II, the CM of the cockpit is always located inside the quadrangle composed of $\mathbf{P}_1, \mathbf{P}_2, \mathbf{P}_3$, and \mathbf{P}_4 with minimum distance among k_i . Similarly, the eccentric margin K of the motion platform II can be calculated from (17) and (17a), whereas different relation $i = i + 3$ for all configurations of L_i ($i = 1, 2, 3, 4$) satisfying constraint (3) as shown in Fig. 2.

D. Dynamic Analysis

Dynamic equations of the motion of the motion platform are derived in (18) by applying Lagrangian formulation in terms of Euler angles (ϕ, θ, ψ). The 3-2-1 coordinate transformation from the inertial to the body frame is applied for dynamic analysis

$$\mathbf{M}\dot{\mathbf{q}}_2 + \mathbf{C}(\mathbf{q}_1, \mathbf{q}_2) + \mathbf{C}_\nu = \mathbf{T}_{\text{ext}} + \mathbf{G} \quad (18)$$

where

$$\mathbf{M} = \begin{bmatrix} \mathbf{I}_R + \mathbf{I}_T & \mathbf{M}_T \\ \mathbf{0}_{3 \times 3} & m\mathbf{I}_{3 \times 3} \end{bmatrix} \text{ and } \mathbf{C}(\mathbf{q}_1, \mathbf{q}_2) = [\mathbf{C}_R(\mathbf{q}_1, \mathbf{q}_2)^T + \mathbf{C}_T(\mathbf{q}_1, \mathbf{q}_2)^T \mathbf{0}_{1 \times 3}]^T$$

where m is the mass of the cockpit, and $\mathbf{q}_1 = [\phi \theta \psi x y z]^T$ and $\mathbf{q}_2 = \dot{\mathbf{q}}_1$

$$\mathbf{I}_R = \begin{bmatrix} -I_a S_\theta & 0 & I_a S_\theta^2 + I_t C_\theta^2 \\ 0 & I_t & 0 \\ I_a & 0 & -I_a S_\theta \end{bmatrix} \text{ and } \mathbf{C}_R(\mathbf{q}_1, \mathbf{q}_2) = \begin{bmatrix} 2(I_a - I_t)S_\theta C_\theta \dot{\theta} \dot{\psi} - I_a C_\theta \dot{\phi} \dot{\theta} \\ (I_t - I_a)S_\theta C_\theta \dot{\psi}^2 + I_a C_\theta \dot{\phi} \dot{\psi} \\ -I_a C_\theta \dot{\theta} \dot{\psi} \end{bmatrix}.$$

\mathbf{C}_ν includes the viscous friction and motor brake; \mathbf{T}_{ext} and \mathbf{G} are the torque and forces by the motors and gravity, respectively; I_a and I_t are the moments of inertia along the x and y axes due to the symmetry of the cockpit and the z -axis in the body frame, respectively; C and

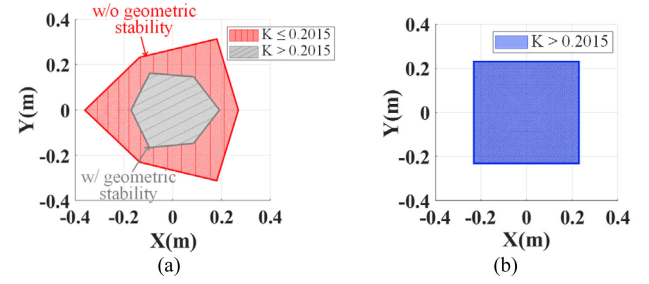


Fig. 3. Workspace for translation. (a) Previous motion platform I [12]. (b) Proposed motion platform II.

S indicate the cosine and sine functions of the subscript Euler angles. \mathbf{I}_T , \mathbf{M}_T , and $\mathbf{C}_T(\mathbf{q}_1, \mathbf{q}_2)$ are the nonlinear terms, which are coupled rotation, caused from the translation.

IV. NUMERICAL SIMULATION AND EXPERIMENTS

The kinematic models of the rotation and translation including coupled motion are applied to validate the design and performance of motion control of both motion platforms I and II. The numerical simulation shows the workspace considering the geometric stability and motion capability of each motion platform. The friction coefficient and slip ratio are evaluated to validate the rolling of the cockpit from experiments. Finally, experiments for the cockpit orientation and active driving control are implemented in an open-loop control and compared to simulation and experiments acquired from [12]. First, control performance of the cockpit is compared when the cockpit is controlled in two different positions: symmetric case ($L_1 = L_2 = L_3 = L_4$) and asymmetric case ($L_1 = L_2 \neq L_3 = L_4$). Second, position along three arbitrary axes is controlled for the motion platform I to improve and compare the coupled rotation due to the translation. The coupled motion is compensated with the active driving control and the results are compared in [12].

A. Numerical Simulation About Motion Capability

Geometric stability and operation space are evaluated from (16) and (17), where K for each platform is calculated with possible operation range L_i satisfying the limit in (5). The results satisfy $K \geq 0.0122$ m for the platform I/0.2015 m for the platform II, respectively. The motion platform II has a larger eccentric margin and becomes more stable and uniform in range of motion than the platform I. The results of eccentric margin can be applied to the workspace of the translation of the cockpit. Fig. 3 shows the comparison of workspace about the XY plane for the motion platforms I and II. The workspace of the platform I is computed with and without geometric stability for comparison to the motion platform II. If the motion platforms I and II have same eccentric margin as 0.2015 m by applying geometric stability, the workspace about the motion platform I is reduced from 0.024 (red + gray region) to 0.0073 m³ (gray region), as shown in Fig. 3(a). The red region where $K \leq 0.2015$ m for the motion platform I is eliminated, as shown in Fig. 3(a). As a result, the reachable workspace of the motion platform I become gray region smaller than the motion platform II. Furthermore, the workspace has asymmetric workspace along the X -axis limiting the motion capability by geometric characteristics, whereas symmetric workspace along the Y -axis. In contrast, the motion platform II has the symmetric and uniform workspace along the X and Y axes with volume 0.0202 m³, which is larger than the motion platform I, as shown in Fig. 3(b).

TABLE I
PERFORMANCE COMPARISON OF THE PLATFORMS I [12] AND II

Rotation of Design I / II	ϕ	θ	ψ
Max. angle (°)	± 180	± 90	± 180
Max. velocity (°/s)	$\pm 32.3/43.6$	$\pm 37.4/43.6$	$\pm 57.6/76.8$
Translation of Design I / II	X	Y	Z
Max. displacement (m)	$\pm 0.18/0.33$	$\pm 0.17/0.33$	$0.25/0.3$
Max. velocity (m/s)	$\pm 0.5/1$	$\pm 0.58/1$	$\pm 0.57/1.1$

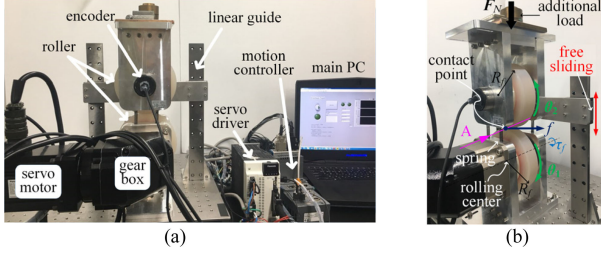


Fig. 4. Experimental setup for friction test. (a) Friction experimental setup. (b) Side view.

Table I lists larger motion capability with geometric stability compared to [12]. The operation limits are computed from the kinematics using (7), (10)–(12) assuming no energy loss by slip.

B. Experiments for Friction Coefficient and Slip Ratio

The main driving force of the motion platform is friction force generated at the contact points and slipping may be occurred causing an imperfect transfer of the torque. Thus, friction and rolling conditions according to the slip ratio are evaluated. Fig. 4 shows the experimental setup. A motor and gearbox are utilized to rotate the lower roller counter-rotating the upper roller. Springs are installed to make the two rollers to be initially balanced at neutral position with zero normal force F_N . Moreover, the linear guide enables an additional load to change the normal force sliding freely along the vertical direction, as shown in Fig. 4(b). MSMF152L1G5 and MDDL755SF are selected as the servo motor including encoder and driver; ABR115-020 is selected as gearbox with 20:1 gear ratio; NI cRIO-9082 is used as the motion controller.

Two rollers in the experiment are made up of the same urethane material compared to small spheres and the cockpit sphere of the prototype motion platform to evaluate the friction coefficient μ and slip ratio λ . It is assumed that the point contact between two rollers in the rolling plane [in cross-sectional view, A as shown in Fig. 4(b)] although the contact is line contact. The friction force $f (= \mu \cdot F_N$ where μ and F_N are a friction coefficient and a normal force, respectively) can be calculated from the motor torque $\tau_f (= f \cdot R_f$ where R_f is radius of roller) where static and kinetic friction coefficients, which are μ_s and μ_k , are 0.355 and 0.118, respectively. The slip ratio λ is experimentally analyzed and the results are shown in Fig. 5. At the initial state with no load except the weight of the upper roller, which is count balanced by springs, only slipping motion occurs. As more loads increase, higher normal force F_N is applied and the slip ratio decreases. Slipping and rolling motion simultaneously occurs at $F_N < 10.75$ N. From $F_N \geq 10.75$ N, it is observed that pure rolling only occurs. The weight of the prototype cockpit is 98 N and the normal force at each contact point between the cockpit and small sphere is larger than 10.75 N sufficiently. The actual contact between the cockpit and small sphere is surface since the urethane material has elastic

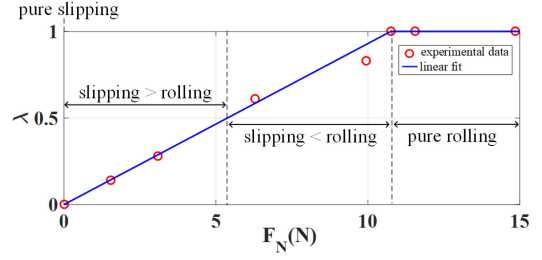


Fig. 5. Slip ratio λ according to the normal force F_N .

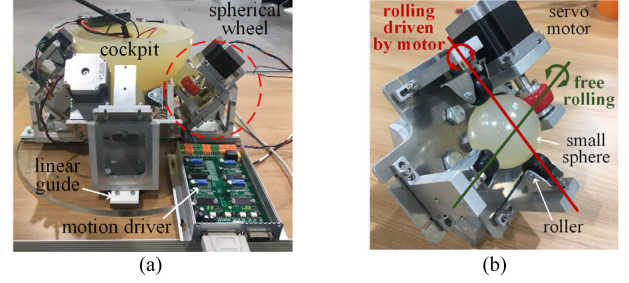


Fig. 6. Prototype of the motion platform II. (a) Side view. (b) Spherical wheel.

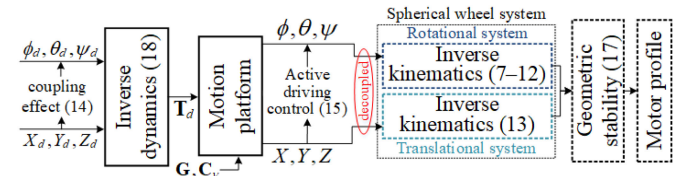


Fig. 7. Open-loop control and overall systems [12].

property, but the weight of the cockpit is large enough to minimize slipping. As a result, the cockpit sphere can rotate minimizing slipping since the torque is less than τ_f within operational acceleration.

C. Experiments for Orientation and Active Driving Control

The orientation of the motion platform II is demonstrated from the prototype with four spherical wheels, as shown in Fig. 6. The active driving control is verified from the actual model in [12] to compare the earlier experimental to the new compensated results. The control is implemented in an open loop satisfying the geometric stability and applying an active driving control as shown in Fig. 7.

1) Orientation Control for Two Cases: For the experiment, the cockpit sphere, small spheres, and rollers are made up of urethane material with hardness of 95 to minimize slipping motion between spheres. Four step motors are used for orientation control to rotate each small sphere generating the torque. The torque is transferred from the small spheres to the cockpit through each contact covering full rotational range along all axes. Four linear stages are installed each linear guide and can generate the translational motion of the cockpit according to movement of stages shown in (4) and (13). 23HM22-2804S and SSELBW16-190 are selected as the step motor which has 400 pulse/rev resolution and linear guide, respectively. TB6560 is utilized as motion driver, and the ratio of microstepping is set to be 1/16 for fine control.

TABLE II
PARAMETERS OF PROTOTYPE FOR EXPERIMENTS

Symmetric case	$L_1=0.101\text{m}$, $L_2=0.101\text{m}$, $L_3=0.101\text{m}$, $L_4=0.101\text{m}$
Asymmetric case	$L_1=0.101\text{m}$, $L_2=0.101\text{m}$, $L_3=0.116\text{m}$, $L_4=0.116\text{m}$
Mass and radius of cockpit sphere:	$M=10\text{kg}$ and $R=0.1075\text{m}$
Radius of roller and small sphere:	$r_s=0.0305\text{m}$ and $r_w=0.0187\text{m}$
Desired angular speed and acceleration (deceleration):	$\omega_d = 6^\circ/\text{s}$ and $\alpha_d = 6^\circ/\text{s}^2$

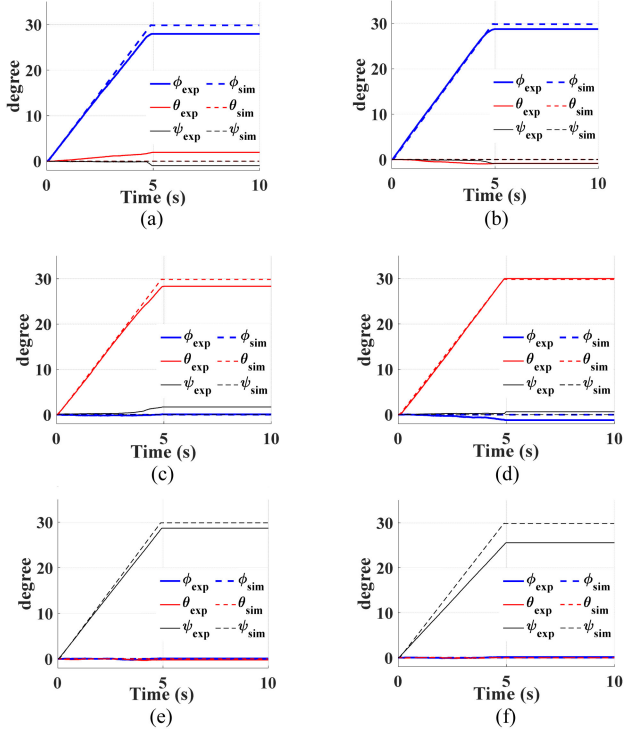


Fig. 8. Comparisons of the rotational motion for the motion platform II. (S indicates symmetry and AS asymmetry). (a) $\phi = 30^\circ$ (S). (b) $\phi = 30^\circ$ (AS). (c) $\theta = 30^\circ$ (S). (d) $\theta = 30^\circ$ (AS). (e) $\psi = 30^\circ$ (S). (f) $\psi = 30^\circ$ (AS).

Experiments for the orientation control are implemented with two configurations of the cockpit sphere with respect to four small spheres. Each case is composed of three independent rotational motions. In arbitrary symmetric and asymmetric cases, L_i ($i = 1, 2, 3, 4$) and other parameters are detailed in Table II. The four motors for the rotation are controlled by using MACH3 software. MW-AHRSv1 is selected for the inertial measurement unit to measure the orientation of the cockpit sphere using wireless network, Xbee module, at 10 Hz sampling rate. In each case, ϕ , θ , and ψ are controlled independently based on kinematics, and each command is a 30° step input for the orientation control. The desired angular position, velocity, acceleration, and deceleration for each motor are set as given in Table II and solved from the inverse kinematics in (7), (10)–(12).

Fig. 8 shows the comparison of the cockpit orientation between the simulation and experiment. In the symmetric, as shown in Fig. 8(a), (c), and (e), the experimental results show the rotational motion which can be independently controlled along each axis. The maximum error is less than 3° and the error is mainly caused due to the accumulation of small slipping, mechanical imperfections, and inaccuracy of the measurement sensor. Similarly, in the asymmetric, the control is also accurate, as shown in Fig. 8(b), (d), and (f), with maximum error less than 5° , slightly larger than the symmetric case. The errors could be

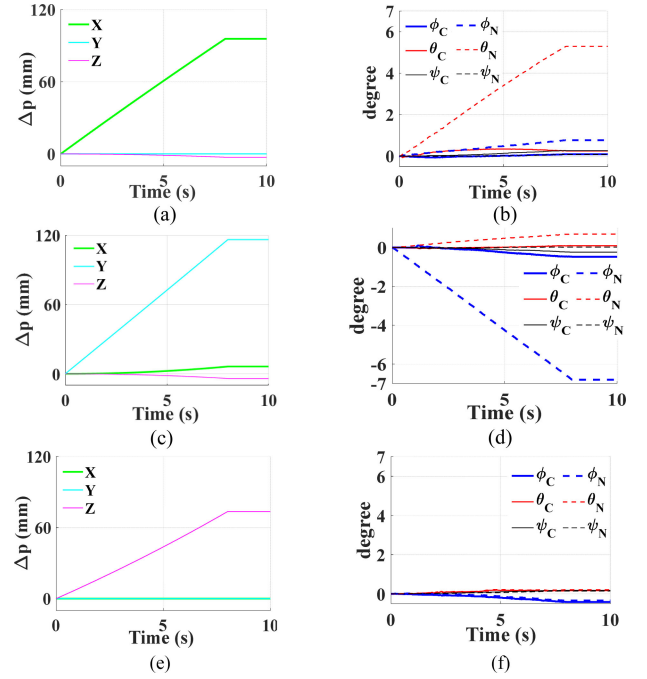


Fig. 9. Comparisons of the translation and rotation according to motion coupling for the motion platform I. (C indicates compensation and N no compensation). (a) $X = 95.7\text{ mm}$ and $Z = -2.8\text{ mm}$. (b) Rotation due to translation. (c) $X = 6.4\text{ mm}$, $Y = 116.2\text{ mm}$. (d) Rotation due to translation. (e) $Z = 73.5\text{ mm}$. (f) Rotation due to translation.

compensated by a closed-loop control for the orientation and position of the cockpit.

2) Active Driving Control: The rotation due to the translational motion is validated by experimental results with and without the active driving control. The experiment is implemented with three arbitrary cases to guarantee motion feasibility and each input command (mm) for the movement of the linear stage is applied as $[100 \ 50 \ 50]^T$, $[0 \ 100 \ -100]^T$, and $[100 \ 100 \ 100]^T$ for Fig. 9(a), (c), and (e), respectively. The desired velocity (mm/s) is set to be $[12.5 \ 6.25 \ 6.25]^T$, $[0 \ 12.5 \ 12.5]^T$, and $[12.5 \ 12.5 \ 12.5]^T$. The desired acceleration and deceleration for each motor are set to be 200 mm/s^2 for fast response. The linear stage moves 5 mm according to 1 revolution (= 10 000 input pulse) of the motor.

The results of the experiment with the active driving control are shown in Fig. 9(b), (d), and (f) according to the translation of the cockpit as shown in Fig. 9(a), (c), and (e), respectively. The coupled rotation angle according to the translation is estimated from (14), and compensated from forward kinematics. The maximum error with the control compensation is smaller than 0.47° . The comparison results show the coupled motion along ϕ and θ axes compensated from the active driving control in real time, although small errors occurred due to mechanical imperfections, slipping, etc. Similarly, the compensation can be applied to platform II by utilizing (14) with $N_a = 4$, and finally, the coupled motion can be eliminated.

V. CONCLUSION

This paper presented the development of a 6-DOFs motion platform based on four spherical wheels, capable of 3-DOFs unlimited rotation and 3-DOFs translation compared to earlier design. The motion platform has higher motion capability and larger workspace for linear motion compared to the previous. In particular, the control

had coupled motion between the translation and rotation, resulting in an intrinsic rotation while translation. Active driving control was developed to compensate motion coupling by kinematics and validated from experiments in an open loop. Moreover, it was experimentally validated that the motion platform can be driven according to the design characteristics and kinematics. The open-loop control also demonstrated motion feasibility of the motion platform. Therefore, it can be utilized to explore various applications such as motion simulator for virtual reality.

REFERENCES

- [1] D. Lee and T. Seo, "Lightweight multi-DOF manipulator with wire-driven gravity compensation mechanism," *IEEE/ASME Trans. Mechatron.*, vol. 22, no. 3, pp. 1308–1314, Jun. 2017.
- [2] C. Viegas, M. Tavakoli, P. Lopes, R. Dessi, and A. T. de Almeida, "SCALA—A scalable rail-based multirobot system for large space automation: Design and development," *IEEE/ASME Trans. Mechatron.*, vol. 22, no. 5, pp. 2208–2217, Oct. 2017.
- [3] M. Kühne, J. Potzy, R. García-Rochín, P. van der Smagt, and A. Peer, "Design and evaluation of a haptic interface with octopod kinematics," *IEEE/ASME Trans. Mechatron.*, vol. 22, no. 5, pp. 2091–2101, Oct. 2017.
- [4] M. T. Pham, T. J. Teo, S. H. Yeo, P. Wang, and M. L. S. Nai, "A 3-D printed Ti-6Al-4V 3-DOF compliant parallel mechanism for high precision manipulation," *IEEE/ASME Trans. Mechatron.*, vol. 22, no. 5, pp. 2359–2368, Oct. 2017.
- [5] Y. Jiang, T. Li, and L. Wang, "Novel method for designing high precision parallel kinematic machines based on the smart structure," *IEEE/ASME Trans. Mechatron.*, vol. 22, no. 4, pp. 1889–1902, Aug. 2017.
- [6] H. Jamshidifar, A. Khajepour, B. Fidan, and M. Rushton, "Kinematically-constrained redundant cable-driven parallel robots: Modeling, redundancy analysis, and stiffness optimization," *IEEE/ASME Trans. Mechatron.*, vol. 22, no. 2, pp. 921–930, Apr. 2017.
- [7] L. Wang, J. Wu, J. Wang, and Z. You, "An experimental study of a redundantly actuated parallel manipulator for a 5-DOF hybrid machine tool," *IEEE/ASME Trans. Mechatron.*, vol. 14, no. 1, pp. 72–81, Feb. 2009.
- [8] H. Cheng, Y.-K. Yiu, and Z. Li, "Dynamics and control of redundantly actuated parallel manipulators," *IEEE/ASME Trans. Mechatron.*, vol. 8, no. 4, pp. 483–491, Dec. 2003.
- [9] H. Son and K.-M. Lee, "Open-loop controller design and dynamic characteristics of a spherical wheel motor," *IEEE Trans. Ind. Electron.*, vol. 57, no. 10, pp. 3475–3482, Oct. 2010.
- [10] Z. Copeland, B. Jung, M. J. D. Hayes, and R. G. Langlois, "Full-scale atlas motion platform: Structures; actuation; control," *Int. J. Mech. Robot. Syst.*, vol. 3, no. 2/3, pp. 94–112, Dec. 2016.
- [11] D. Stewart, "A platform with 6 degrees of freedom," *Proc. Inst. Mech. Eng.*, vol. 180, pp. 371–386, 1965.
- [12] S.-M. Lee and H. Son, "Multidegree-of-freedom motion platform based on spherical wheels," *IEEE/ASME Trans. Mechatron.*, vol. 22, no. 5, pp. 2121–2129, Oct. 2017.
- [13] S.-M. Lee and H. Son, "Six DOFs motion platform using omni-spherical wheels," in *Proc. IEEE/ASME Int. Conf. Adv. Intell. Mechatron.*, 2018, pp. 427–431.